Hierarchical meta-porous materials as sound absorbers

S. Kuznetsova, Samuel Deleplanque, Florian Allein, Bertrand Dubus, M. Miniaci

PROCEEDINGS A

royalsocietypublishing.org/journal/rspa

Research

Cite this article: Kuznetsova S, Deleplanque S, Allein F, Dubus B, Miniaci M. 2024 Hierarchical meta-porous materials as sound absorbers. *Proc. R. Soc. A* **480**: 20230831. https://doi.org/10.1098/rspa.2023.0831

Received: 10 November 2023
Accepted: 23 September 2024

Subject Category:
Physics

Subject Areas:
acoustics, civil engineering

Keywords:
hierarchical metamaterials, low-frequency absorption, porous materials, transfer matrix method, finite-element method, multi-scale organization

Author for correspondence:
Marco Miniaci
e-mail: marco.miniaci@gmail.com

One contribution to a special feature 'Asymptotic and numerical models of acoustic, thermal and elastodynamic metamaterials' organised by Sébastien Guenneau, Agnes Maurel and Kim Pham.

Electronic supplementary material is available online at https://doi.org/10.6084/m9.figshare.c.7477906.

THE ROYAL SOCIETY PUBLISHING

Hierarchical meta-porous materials as sound absorbers

Svetlana Kuznetsova, Samuel Deleplanque, Florian Allein, Bertrand Dubus and Marco Miniaci

Univ. Lille, CNRS, Centrale Lille, Junia, Univ. Polytechnique Hauts-de-France, UMR 8520 - IEMN - Institut d'Electronique de Microélectronique et de Nanotechnologie, Lille F-59000, France

MM, 0000-0002-6830-3548

The absorption of sound has great significance in many scientific and engineering applications, from room acoustics to noise mitigation. In this context, porous materials have emerged as a viable solution towards high absorption performance and lightweight designs. However, their performance is somewhat limited in the low-frequency regime. Inspired by the concept of recursive patterns over multiple length scales, typical of many natural materials, here, we propose a hierarchical organization of multilayered porous media and investigate their performance in terms of sound absorption. Two types of designs are considered: a hierarchical periodic (HP) and a hierarchical gradient (HG). In both cases, it is found that in some frequency ranges the introduction of multiple levels of hierarchy simultaneously allows for: (i) an increase in the level of absorption compared with the corresponding bulk block of porous material (or to the previous hierarchical levels (HLs)), and (ii) a reduction in the quantity of porous material required. Another advantage of using this approach is on the fabrication, since only one porous material is required. The performances are examined for both normal and oblique incidences, as well as for different values of the static air-flow resistivity. The methodological approach is based on the transfer-matrix method, optimization algorithms such as the metaheuristic greedy randomized adaptive search procedure (GRASP), finite-element calculations and measurements performed in an impedance tube.

1. Introduction

One of the stumbling blocks in modern acoustics is the absorption of sound at low frequencies, especially when the thickness of the absorbing structure is smaller than the wavelength of the incident sound wave. This performance, highly desirable in most noise shielding applications related to human activities, is even more chased in contexts such as room acoustics, engine noise control and, in general, where the space hosting the absorber is limited [1].

In this context, porous materials have emerged as a viable solution towards high absorption performance and lightweight designs [2,3]. The main mechanism responsible for sound absorption in porous media derives from the conversion of sound energy into heat, further dissipated through the large number of complex micro-pores of which these materials are composed [4]. Several theoretical models have been proposed to describe their acoustic behaviour [5–8]. Among them, the Johnson–Champoux–Allard (JCA) model is probably the most widely used [9–11]. It describes the porous media through five physical parameters, namely: (i) static air-flow resistivity σ, (ii) open porosity ϕ, (iii) tortuosity α_∞, (iv) viscous characteristic length Λ and (v) thermal characteristic length Λ'.

Porous materials exhibit good absorption at medium and high frequencies, whereas their performance is somewhat limited in the low-frequency regime [12]. To overcome this deficiency without increasing their overall thickness, specific designs of porous materials, also known as 'meta-porous materials' or 'porous metamaterials', have recently been proposed [13]. The most common approaches include: (i) introducing resonators into the porous media generating additional peaks of absorption at the desired (low-) resonance frequencies of the resonator [14–16]; (ii) inserting a set of rigid partitions into the porous media responsible for the formation of multiple slow waves propagating over the full layer thickness. Specifically, this approach proved to be very effective in enhancing the absorption in the low-frequency regime with respect to the corresponding block of bulk porous material, though performances in the middle and high frequencies [17,18]; (iii) topological optimization of the porous materials including air cavities [19,20] and micro-perforated panels [21,22]; (iv) multi-scale design of porous materials with slits [23,24] and holes [25] allowing for sound waves with longer wavelengths to enter the material and be dissipated; (iv) multilayered porous media, whose overall dynamic performance strongly depends on the geometrical arrangement of the constituent elements.

Initiated in the early 1990s [26–28], the meta-porous approach is again attracting increasing interest in the scientific community owing to recent developments in acoustic metamaterials [29,30] and fabrication techniques [31], which have allowed for the conception of new designs more and more optimized [32,33] for an efficient and broadband sound attenuation at low frequencies using moderate amounts of absorbing materials [13]. In this context, Jimenez *et al*. [34] proposed an optimized chirped multilayered porous material exhibiting enhanced low-frequency absorption (compared with that of the corresponding bulk porous material of the same length). The sound absorption and transmission of the system were theoretically analysed, revealing unidirectional performances, given the broken geometrical symmetry introduced by the chirped design. Optimized layers of porous materials have also shown promise of reaching perfect and broadband sound absorption [35]. In this case, the performance enhancement derived from the impedance matching of the meta-porous material to the incoming wave. Another example of gradient variation of the material properties is structure with dual porosity, where gradually increasing the number of additional perforations significantly increases the absorption [36]. Furthermore, adjusting the shape of the perforations is of crucial importance for achieving high absorption values [37]. Almeida *et al*. [38] investigated a multilayered porous material with slit-type perforations organized according to the Cantor set, i.e. exhibiting a fractal porosity. A broadband and efficient absorption performance in the low-frequency regime was reported.

Despite the large number of meta-porous designs proposed so far, enhancing the absorption performance of these materials at low frequencies remains an open research issue. In this

context, the concept of hierarchy, borrowed from Nature, has recently emerged as a promising source of inspiration for the engineering of metamaterials with complex structural architectures leading to advanced functional properties in several research fields, from electromagnetism to elasticity and acoustics [39–45]. Hierarchical architectures, which can be defined as recursive structural patterns repeated at different length scales, are widespread in nature, being a developmental outcome of coping with evolutionary challenges, often bringing to enhanced and functional-oriented properties compared with simpler structural organizations [46]. Initially, mainly investigated in the quasi-static domain, hierarchical architectures have also recently gained increasing interest in dynamics and in acoustic metamaterials. For instance, Li *et al*. [47] showed that adding surface porosity and unit-cell heterogeneity in a multi-scale structure inspired by the cuttlefish bone allows for broadband sound absorption and a higher deformation tolerance. A spider-web-like organization [48] or hierarchical honeycomb arrangements [49,50] revealed improvements in bandgap properties, while acoustic metamaterials made of hierarchical membranes can achieve unusual transmission loss characteristics [51]. A sandwich structure with a hierarchical honeycomb interior has been shown to enhance the absorption in a much wider frequency range as compared with the regular sandwich [52]. Finally, labyrinthine fractal acoustic structures have recently shown increased low-frequency sound attenuation [53] and reflection [54]. Moreover, hierarchy in the reciprocal space, i.e. hierarchical band gaps, has recently been reported in complex periodic structures [55].

Here, we introduce the concept of hierarchical meta-porous materials, i.e. multilayered stacks of porous material and air, the geometrical organization of which describe a family of self-replicating structures (with or without exact self-similarity [56]) at different length scales (see figure 1). Through analytical calculations based on the transfer-matrix method, optimization algorithms such as the metaheuristic greedy randomized adaptive search procedure (GRASP), finite-element simulations and measurements at normal incidence in an impedance tube, we demonstrate the enhancement of the absorption coefficient as additional hierarchical levels (HLs) are added to the porous layers(s). Two types of organization are investigated, and their performance is compared to that of the corresponding block of bulk material (or to the previous HLs): a hierarchical periodic (HP) and a hierarchical gradient (HG). In both cases, it is found that in some frequency ranges the introduction of multiple levels of hierarchy simultaneously allows for: (i) an increase in the level of absorption and (ii) a reduction the quantity of porous material required to achieve better performance. Both cases of normal and oblique incidences are examined, as well the influence of static air-flow resistivity, which, among all the JCA model parameters, appeared to be the most influential on absorption in the considered frequency range. An optimization procedure has been applied to maximize the absorption of the highest HL in the desired frequency range (20–2000 Hz), since for each proposed structure adding further HLs is always possible.

We note that our HP and HG designs are inspired by comprehensive works [34,35,57]. In Zhang *et al*. [57], the proposed structure is made of alternating soft and hard elastic materials (hydroxyapatite and protein) immersed in water, where no optimization is performed. In Jiménez *et al*. [34], porous and air layers are considered and the optimization is driven by the search for perfect absorption, while Jiménez *et al*. [35] used quarter-wavelength resonance with the goal of deriving the optimal (reference) length of the structure based on this condition, thus leading to a stack of only porous layers with different lengths and air-flow resistivity. In contrast, the goal of our study is to investigate how applying the (same) rationale of 'introducing additional hierarchical arrangement of unit cells' can achieve a performance enhancement of perfectly periodic or gradient multi-layered structures in some frequency or static air-flow resistivity ranges.

The paper is organized as follows: §2 is devoted to the description of the models and methods. First, the HP and the HG designs are introduced, then the type of model adopted to describe the porous layers and the formalism used to calculate their absorption properties are provided. Finally, the details of the optimization algorithm exploited to define the designs are

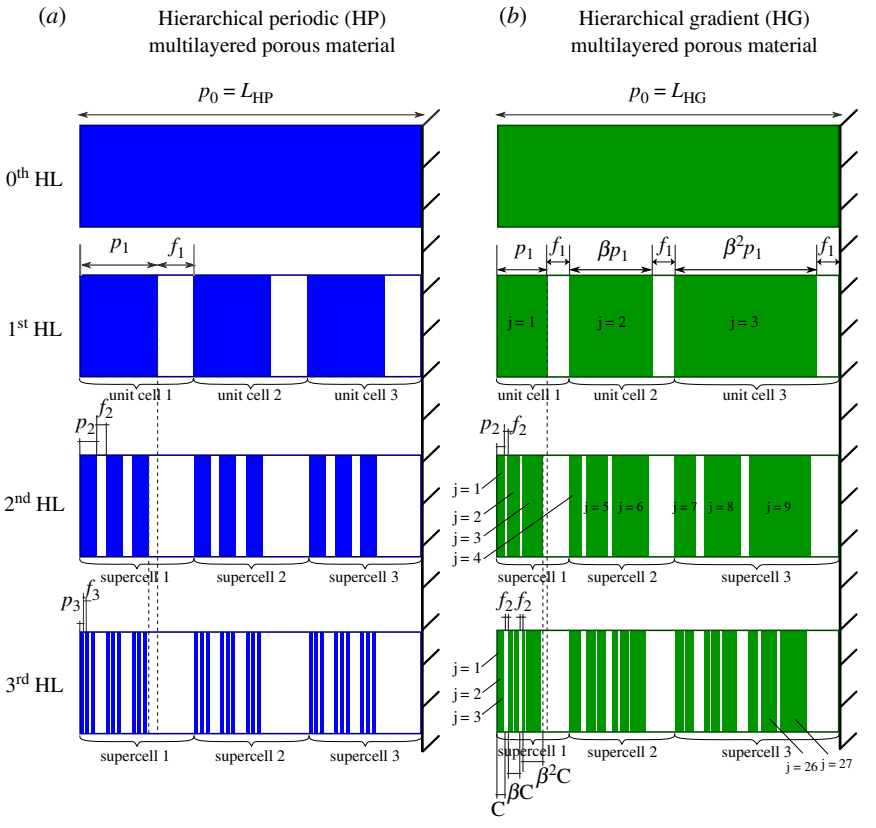

Figure 1. HP and HG multilayered porous structures. (*a*) A HP multilayered porous structure. The porous layers are coloured blue, and the air gaps in white. (*b*) A HG multilayered porous structure. The porous layers are coloured green, and the air gaps in white. In both cases, $m = 3$ HLs are investigated, and the simplest organization, the 0th HL, reduces to a bulk block of porous material. The recursive rule to build each next HLs ith , with $i \in [1, m]$, is to divide the porous domain(s) of the previous level $(i-1)$th of length p_{i-1} in $n = 3$ porous and air layers. In (*a*), the resulting layers have constant lengths p_i and f_i throughout the sample, while in (*b*), the structure self-replicates following the scaling rule $p_i^{(j)} = p_i \beta^{j-1-(n-1)\sum_{q=1}^{i-1}\left[\frac{j-1}{n^q}\right]}$, where β is a constant parameter, $i \in [0, m]$ the considered HL, $j \in [1, n \times m]$ the porous-layer sequence number, p_i the length of the first porous layer of the ith HL and $[\,\cdot\,]$ indicates the integer part of the number included within the square brackets.

given. In §3 we report the results for the cases of normal and oblique plane wave incidence, as well as the effect of the static air-flow resistivity on the absorption coefficients. Section 4 is devoted to the experimental validation of the results. Conclusions and further perspectives are given in §5.

2. Models and methods

(a) HP and HG design

A great variety of biological systems exhibit hierarchical organization, i.e. recursive geometrical patterns repeating at the micro- and/or macro-scales [58]. Hierarchy often derives from heterogeneity introduced in the form of: (i) reinforcing elements (fibres, platelets or crystals embedded in a softer matrix), (ii) voids, cavities or canals in a matrix and/or (iii) alternating layers of stiffer and softer materials [41]. These diverse organizations can contribute to

royalsocietypublishing.org/journal/rspa Proc. R. Soc. A 480: 20230831

increased energy dissipation and crack deflection capabilities, toughness and resilience [59], but can also potentially affect the propagation of elastic waves or damping along with an overall mass density reduction [60]. Indeed, the evidence for a strong correlation between the propagation of waves and the micro-structure of the biocomposites hosting the propagation has been shown, connecting it to the hierarchical organization, often consisting of hard material building blocks embedded in a soft organic matrix, assembled in a hierarchical manner across multiple length scales [57]. Hierarchy can occur at different length scales, as in bones, nacre or, at similar length scales, as in leaves, wood, corals or sponges (porous materials) [61,62]. Electron microscope images of such hierarchical structures have often shown that their micro-structure appears not only to be self-similar but also periodic at each level of their structural hierarchy, such as in the case of enamel and dentine, protecting our teeth from failure after millions of times of mastication, or lobster cuticles, shrimp clubs and crab claws exhibiting exceptional resistance to repeated dynamic attack either for preying or shielding purposes [63].

Inspired by these patterns, we propose and investigate a multilayered porous media with a: (i) HP and (ii) HG organization, as shown in figure 1. In our case, the stiffer layers (coloured blue for HP and green for HG) are made of porous material (polyurethane), whereas the softer ones (shown white) of air. In both cases, $m = 3$ HLs are investigated, and the simplest organization, the 0^{th} HL, reduces to a bulk block of porous material of length p_0 (top panels of figure 1), where $p_0 = L_{\text{HP}} = 260$ mm in the case of HP, and $p_0 = L_{\text{HG}} = 413$ mm in the case of HG.

In the HP study case, the recursive rule adopted to build each next HL i^{th}, with $i \in [1, m]$, is to divide the porous domain(s) of the previous level $(i-1)^{\text{th}}$ of length p_{i-1} in $n = 3$ unit cells (supercells) made of porous and air layers of length p_i and f_i, respectively. For instance, the first HL is made of three unit cells of alternating porous and air layers of length p_1 and f_1 ($p_1 f_1$), such that $n \cdot (p_1 + f_1) = p_0$. In the same manner, the second HL divides each porous domain of length p_1 of the first HL into three unit cells of alternating porous and air layers of length p_2 and f_2, respectively, so that they form three supercells $p_2 f_2 p_2 f_2 p_2 f_2 f_1$ of total length $n \cdot (p_2 + f_2) + f_1 = p_1 + f_1$. Finally, the supercell of the last HL (third HL) consists of the following combination of alternating porous and air layers $p_3 f_3 p_3 f_3 p_3 f_3 f_2 p_3 f_3 p_3 f_3 p_3 f_3 f_2 p_3 f_3 p_3 f_3 p_3 f_3 f_2 f_1$. The parameters m and n have been here arbitrarily chosen to be equal to 3 to maintain a good compromise between a sufficient high number of HLs explored and a limited total length of the structure. Nevertheless, similar reasoning can be applied for higher or lower values of n. The thinnest porous-layer thickness has been limited to at least 4 mm so that the JCA model properly describe its behaviour [9]. The lengths of the porous and fluid layers are determined as a result of an optimization procedure applied to the last HL—see §2*d*.

In the HG study case, the finite structures of each HL (other than the 0th HL, which is a bulk block of porous material) are made of $n = 3$ unit cells (supercells) constituted of porous and air layers (as in the HP case). The difference, here, is that the three unit cells (supercells) belonging to the same HL exhibit different lengths according to the rule

$$p_i^{(j)} = p_i \beta^{j-1-(n-1)\sum_{q=1}^{i-1}\left[\frac{j-1}{n^q}\right]}, \tag{2.1}$$

where β is a constant parameter (determined to be equal to 1.1085 by the optimization algorithm—see §2*d*), $i \in [0, m]$ indicates the HL, $j \in [1, n \times m]$ the porous-layer sequence number, p_i the length of the first porous layer of the ith HL and $[\,\cdot\,]$ indicates the integer part of the number included within the square brackets. The recursive rule to build each next HL ith, with $i \in [1, m]$, is to divide the porous domain(s) of the previous $(i-1)$th HL into n porous and air layers keeping the proportions of the previous HL constants, i.e. maintaining the ratio $\frac{p_i}{f_i}$. More qualitatively, the process can be described as taking all the porous and fluid layers of the whole structure of the $(i-1)$th HL and squeezing them successively into the length(s) corresponding to that (those) of the jth(s) porous layer(s) of the first HL, minus the length(s) of

the last fluid layer(s) of the second to the $(i-1)$th HL(s), to form the $(j-1)n^{i-1}+1$ up to the jn^{i-1} porous layers of the successive ith HL (in this recursive formula, the indices j always refer to the first HL). For instance, the first HL is made of $n=3$ unit cells of alternating porous and air layers of lengths $p_1, f_1, \beta p_1, f_1, \beta^2 p_1, f_1$, such that $p_1 \cdot \sum_{i=1}^{n} \beta^{i-1} + n \cdot f_1 = p_0$. In the same manner, the second HL divides each porous domain jth of the first HL into $n=3$ alternating porous and air layers of lengths $p_2^{(t)}$ and $f_2^{(t)}$, respectively, so that $\sum_{t=1}^{n}(p_2^{(t)} + f_2^{(t)}) = p_1^{(j)}$. Finally, the last HL (the third one) appears to be constructed from the supercells $C = p_3, f_3, \beta p_3, f_3, \beta^2 p_3, f_3$ illustrated in figure 1*b* in the following sequence

$$\begin{aligned} &C, f_2, \beta C, f_2, \beta^2 C, f_2, f_1, \\ &\beta C, \beta f_2, \beta^2 C, \beta f_2, \beta^3 C, \beta f_2, f_1, \\ &\beta^2 C, \beta^2 f_2, \beta^3 C, \beta^2 f_2, \beta^4 C, \beta^2 f_2, f_1 . \end{aligned} \tag{2.2}$$

(b) Modelling of the porous material

The porous layers are made of polyurethane, for which the propagation of sound is described through the JCA model [11]. The following parameters are adopted: porosity $\phi = 0.98$, tortuosity $\alpha_\infty = 1.34$, viscous characteristic length $\Lambda = 150$ μm, thermal characteristic length $\Lambda' = 560$ μm and static air-flow resistivity $\sigma = 49\,000$ and $\sigma = 10\,000$ Pa.s m^{-2}. These two values of static air-flow resistivity have been investigated because they are representative of most common porous media. The effective density and bulk modulus of the porous material are expressed as [11,64]

$$\begin{aligned} \rho_p &= \frac{\rho_0 \alpha_\infty}{\phi}\left(1 - \frac{i\omega_c}{\omega}F(\omega)\right), \\ K_p &= \frac{\gamma P_0}{\phi}\left(\gamma - (\gamma-1)\left(1 - \frac{i\omega_c'}{\mathrm{Pr}\omega}G(\mathrm{Pr}\omega)\right)^{-1}\right)^{-1}, \end{aligned} \tag{2.3}$$

where $\omega_c = \frac{\sigma\phi}{\rho_0\alpha_\infty}$ is the Biot frequency, $\omega_c' = \frac{\sigma'\phi}{\rho_0\alpha_\infty}$, $\sigma' = \frac{8\alpha_\infty\eta}{\phi\Lambda'^2}$ [65] is the thermal resistivity [66] and the correction functions are given by [8,67]

$$\begin{aligned} F(\omega) &= \sqrt{1 + i\eta\rho_0\omega\left(\frac{2\alpha_\infty}{\sigma\Lambda\phi}\right)^2}, \\ G(Pr\omega) &= \sqrt{1 + i\eta\rho_0\mathrm{Pr}\omega\left(\frac{2\alpha_\infty}{\sigma'\Lambda'\phi}\right)^2}, \end{aligned} \tag{2.4}$$

where $P_0 = 101.325$ kPa is the atmospheric pressure, and the parameters of air (which is assumed to be the fluid present in the pores) are given by $\rho_0 = 1.204$ kg m^{-3} (density of the air), Pr = 0.71 (Prandtl number), $\gamma = 1.4$ (heat capacity ratio) and $\eta = 1.839 \cdot 10^{-5}$ kg m^{-1} s^{-1}) (air viscosity). Once these parameters are determined, the wavenumber $k_p = \omega\sqrt{\frac{\rho_p}{K_p}}$ and the effective acoustic impedance $Z_p = \sqrt{\rho_p K_p}$ can be obtained.

For the sake of clarity, we note that the JCA is typically considered valid down to approximately 45 Hz. To accurately model the behaviour below this range, low-frequency corrections to the JCA should be considered, such as, for instance, the JCAPL [68].

Although the JCA model is often referred to in the literature as a '5-parameter model', when the micro-structure is changed all the parameters should be adapted to be consistent with the micro-geometry considering these parameters as interconnected, particularly when high frequencies and $\sigma < 10$ kPa·s m^{-2} are concerned. For instance, both Λ and Λ' depend on σ being, in general, correlated by a factor of approximately 2 for cylindrical pores. To take

this interdependence into account, the following relation is adopted among some of the JCA parameters: $8\alpha_\infty\eta/\sigma\phi\Lambda^2 \approx 1$ [11].

(c) Calculation of the absorption coefficient

A harmonic plane wave with time dependence $e^{-i\omega t}$ incident on the rigidly backed multilayered hierarchical structures is considered. The pressure field in each layer obeys the Helmholtz equation $\Delta p + k_j^2 p = 0$, with $k_j = \omega/c_j = k_p(k_0)$ being the wave vector either in the porous or air layer, and c_j being the corresponding speed of sound. The pressure and the velocity are continuous along the structure and the rigid backing imposes the boundary condition $\partial p/\partial x = 0$ at $x = L_{HP}$ or $x = L_{HG}$ (see figure 1). The transfer-matrix formalism is adopted. Let us first consider a single layer of material with density ρ and speed of sound c under the incidence of a plane wave with a wave vector $\vec{k} = (k_x, k_y)$. Separating the variables of the Helmholtz equation as $p(x, y) = p_1(x)p_2(y)$, we can write $d^2p_1/dx^2 + k_x^2 p_1 = 0$, with $k_x = \sqrt{k^2 - k_y^2}$. The particle velocity is defined through the Euler equation $\rho\partial\vec{v}/\partial t = -\nabla p$, leading to $v_x = \frac{1}{k\rho c}\partial p_1/\partial x$. Inside each layer the pressure and velocity are given by

$$p_1 = Ae^{-ik_x x} + Be^{ik_x x}, \tag{2.5}$$

$$v_1 = (Ae^{-ik_x x} - Be^{ik_x x})k_x/kc\rho\,. \tag{2.6}$$

Expressing these quantities at both ends of the layer ($x = 0$ and $x = L$) and discarding the coefficients A, B, one can relate the pressure and velocity at both ends:

$$p_1(L) = \cos(k_x L)p_1(0) - \frac{iZk}{k_x}\sin(k_x L)v_x(0), \tag{2.7}$$

$$v_x(L) = \cos(k_x L)v_x(0) - \frac{ik_x}{Zk}\sin(k_x L)p_1(0), \tag{2.8}$$

where we have introduced the impedance $Z = \rho c$. Reorganizing the relations, one obtains the transfer matrix for a single layer:

$$T = \begin{pmatrix} \cos k_x L & iZ\dfrac{k}{k_x}\sin k_x L \\ \dfrac{i}{Z}\dfrac{k_x}{k}\sin k_x L & \cos k_x L \end{pmatrix}. \tag{2.9}$$

In the multilayered structure, this transfer matrix describes each *jth* layer:

$$T_j = \begin{pmatrix} \cos k_{jx} l_j & iZ_j\dfrac{k_j}{k_{jx}}\sin k_{jx} l_j \\ \dfrac{i}{Z_j}\dfrac{k_{jx}}{k_j}\sin k_{jx} l_j & \cos k_{jx} l_j \end{pmatrix}, \tag{2.10}$$

where l_j is the length of the corresponding layer, $k_{jx} = k_{px}(k_{0x})$ is the projection of the wavenumber perpendicular to the layers, $Z_j = Z_p(Z_0)$ is the impedance and θ is the angle of the incident plane wave considered. The subscripts p and 0 indicate whether the property refers to the porous or fluid (air) layer, respectively. The total transfer matrix $T^{(n)}$ of the nth HL is the consecutive product of the transfer matrices of each layer:

$$T^{(n)} = \prod_j T_j\,. \tag{2.11}$$

The reflection coefficient is obtained from

$$R_n = \frac{T_{11}^{(n)}\cos\theta - Z_0 T_{21}^{(n)}}{T_{11}^{(n)}\cos\theta + Z_0 T_{21}^{(n)}}, \tag{2.12}$$

and the absorption determined as $\alpha_n = 1 - |R_n|^2$.

(d) Optimization of the geometry

For the sake of comparison of the absorption performances of the multilayered structures additional HLs are introduced. The absorption coefficient of the highest HL (third one in our case) is optimized by minimizing the area above the absorption curve $\alpha_3(f)$ in the desired frequency range (20–2000 Hz), without necessarily aiming at perfect absorption in specific frequencies, but rather searching for a global higher absorption performance over the whole frequency range (although the optimization procedure can easily be extended for perfect absorption purposes, as well). The strategy of optimizing the highest HL has been chosen because for a given multilayered structure additional HLs can always be added.

The optimization algorithm adopted is based on the resolution scheme of the metaheuristic GRASP [69]. A solution is constructed, without backtracking, in a very short time (between 1.8 and 2.0 s). According to the type of structure to optimize (HP or HG), a large variety of solutions is obtained through a randomized exploration of the greedy algorithm which assigns values to the variables describing the lengths of the porous (p_3 in the HP and p_3^j in the HG) and fluid (f_i) layers, the number of HLs m, the number of unit cells (supercells) n and/or the evolution coefficient β (this last one concerning the HG study case, only). Restricted by practical requirements, the aforementioned parameters were bounded by $p_i \geq 4$ mm, $f_i \geq 1.8$ mm, $m \leq 3$, $n \leq 3$ in the optimization procedure. The resulting solutions were then sorted based on a 'best absorption' criterion, which forms the objective function.

The choice of a specific algorithm is based on the type of variables being processed, that is, integer or continuous. Methods such as genetic algorithms are particularly effective for integer and/or binary variables [70]. Metaheuristics like particle-swarm optimization are well suited to problems in which continuous variables are considered [71]. In our case, we opted for a two-phase method, allowing for flexible management of different types of variables. Specifically, the first phase consists of a randomized greedy heuristic generating a large number of solutions, among which are those exhibiting the most efficient absorption. Similar to GRASP, we have developed a 'Master–Slave' method where the Master phase involves generating a large number of solutions in a greedy and random manner. Among the best solutions, the integer variables (such as the number of layers, levels of hierarchy, etc.) are fixed. The Slave phase corresponds to a second step that focuses solely on optimizing the continuous variables, which represent the porous/fluid ratio of each cell.

3. Results

In this section, the absorption performances for the cases of normal and oblique plane wave incidence, as well as the effect of the static air-flow resistivity are reported for the HP and HG arrangements. The geometrical parameters issued from the optimization procedure are as follows: $L_{HP} = 260$ mm, $p_3 = 4$ mm, $f_3 = 2$ mm, $f_2 = 6$ mm, $f_1 = 14.7$ mm for the HP case and $L_{HG} = 413$ mm, $p_3 = 4$ mm, $f_3 = 1.8$ mm, $f_2 = 8.4$ mm, $f_1 = 39.4$ mm and $\beta = 1.1085$ for the HG case. The sizes were rounded to the nearest 0.1 mm. This led to the following porous volume reductions (with respect to the 100% porous material of the 0th HL) for the two cases: 17% for the first HL, 37.7% for the second HL, 58.5% for the third HL in the HP organization and 28.6% for the first HL, 47% for the second HL, 58.7% for the third HL in the HG study case. We note that the solution distribution of the optimized geometries are smoothly distributed with respect

to the variation of the porous and air lengths. This confirms the robustness of the hierarchical design with respect to potential geometrical imperfections owing to the manufacturing process. The different lengths p_0 for the HP and HG configurations were caused by the fact that the design is mainly driven by the idea of keeping the samples as compact as possible, once the highest HL is defined (three in our case). Therefore, considering a minimum thickness layer of approximately 4 or 5 mm to correctly use the JCA model [9], in the periodic case, all the layers can be of the same minimal size, whereas in the HG, within the same supercell more room is needed. This leads to a larger p_0 in the HG case as compared with the HP.

(a) HP organization

(i) Normal incidence

Figure 2*a* shows the absorption coefficient α as a function of the frequency f for the HP study case. The comparison includes three HLs in addition to the case of the bulk block of porous material (0th HL) for two different values of σ, 49 000 Pa.s m^{-2} (left-hand panel) and 10 000 Pa.s m^{-2} (right-hand panel), respectively. A plane wave normally incident from the left-hand side of the structures is considered. The results, issued from the transfer-matrix method described in the previous §2b and c, are shown as continuous coloured lines (black for the 0th HL, red for the first HL, blue for the second HL and green for the third HL). The absorption coefficients are also calculated numerically through finite-element methods using the 'Acoustics' module of Comsol Multi-physics, and shown as coloured circular markers (black for the 0th HL, red for the first HL, blue for the second HL and green for the third HL). Perfect agreement is found over the whole frequency range (20–2000 Hz). the left- and right-hand panels of figure 2*a* clearly show that the introduction of hierarchy brings considerable enhancement of the absorption properties of the structure, regardless of the chosen value of σ (49 000 or 10 000 Pa.s m^{-2}). For the first iteration (0th HL $\Longrightarrow$ first HL) the observed variation of α is rather limited, whereas the introduction of additional HLs in porous media with a larger value of σ brings a clearly visible and progressive increase of the absorption coefficient over the whole frequency range considered. The largest enhancement (39%) is reached at f = 75 Hz and an increase between 20% and 25% is observed when $f \geq 200$ Hz, when the third HL is compared with the bulk block of porous material, the 0th HL.

In this case, the enhancement of the absorption coefficient exhibits an oscillating behaviour reaching a maximum enhancement of 20% at f = 330 Hz (where an absorption peak deriving from the $\lambda/4$ resonance is expected). The percentage of the absorption enhancement reduces at higher frequencies.

To obtain further insight into the possible origin of the observed increase in the absorption coefficient as additional HLs are added, the real (left-hand axis, solid lines) and imaginary (right-hand axis, dashed lines) parts of the material impedance (normalized to the impedance of air Z_0) are shown in figure 2*b*. When the larger value of σ is considered (left-hand panel), $\Im(Z/Z_0)$ asymptotically tends to zero as additional HLs are added, whereas $\Re(Z/Z_0)$ tends to one. A similar trend is globally maintained in the case of smaller values of σ (right-hand panel), although with an oscillating behaviour over the frequencies. This means that adding HLs to the design allows for better impedance matching between the absorbing structure and the external medium from which the plane wave is coming (air); perfect absorption occurs when $\Im(Z/Z_0) = 0$ and $\Re(Z/Z_0) = 1$ simultaneously. This justifies the higher absorption observed. We note that, in general, the sample with σ = 10 000 Pa.s m^{-2} provides better impedance matching ($\Im(Z/Z_0)$ closer to zero and $\Re(Z/Z_0)$ closer to one) in the full frequency range under consideration.

To quantify the absorption in the different porous layers composing the hierarchical media, the spatial derivative of the acoustic intensity inside each structure at f = 900 Hz (where

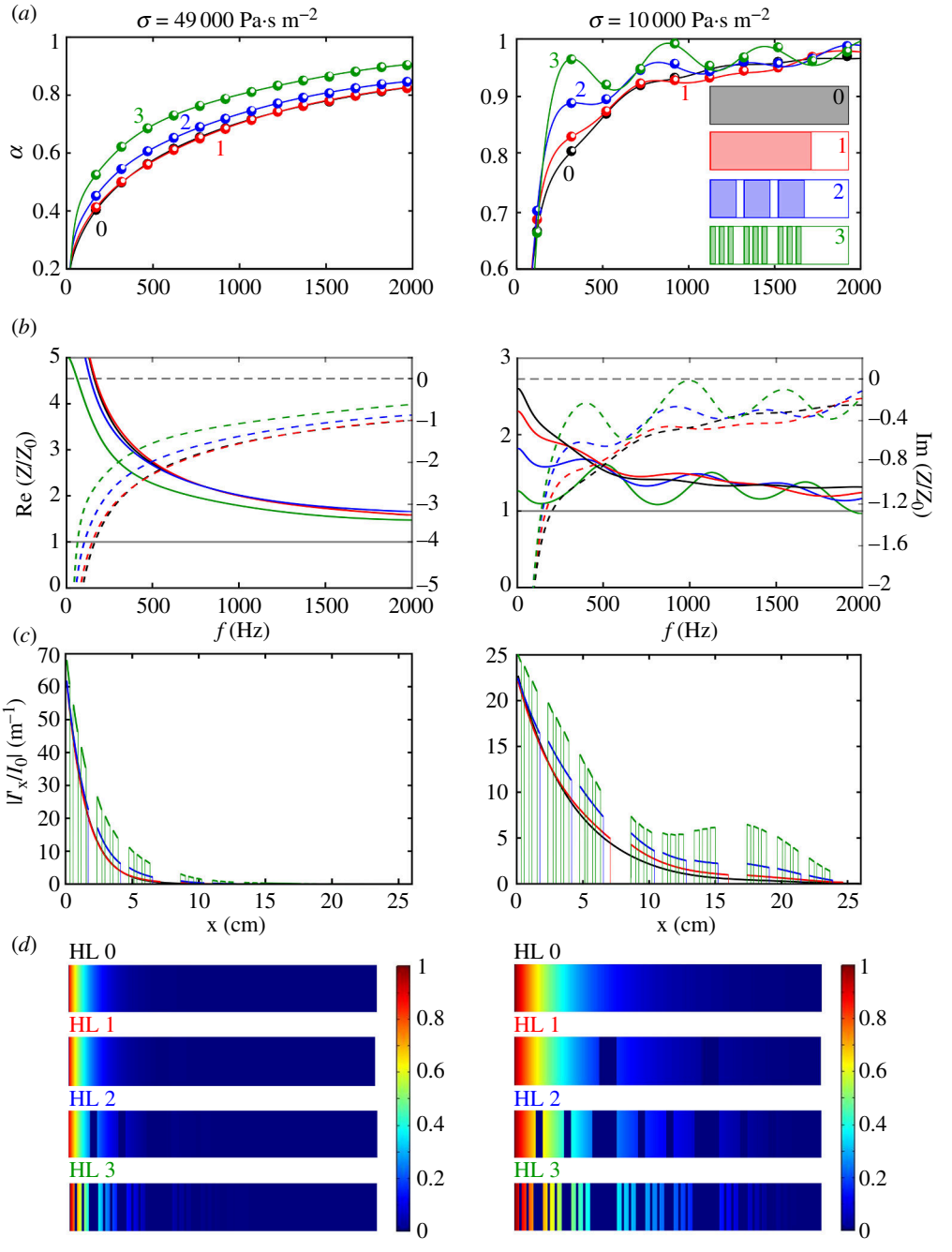

Figure 2. Absorption coefficient, impedance, spatial derivative of the acoustic intensity and the dissipated intensity. (*a*) The absorption coefficient α for different HLs, (*b*) the real (solid lines) and imaginary (dashed lines) parts of the acoustic impedance normalized to that of air, (*c*) the spatial derivative of the acoustic intensity normalized to that at the left-hand end of the structure at $f = 900$ Hz, and (*d*) the dissipated intensity at $f = 900$ Hz. Left-hand panels correspond to $\sigma = 49\,000$ Pa.s m^{-2}, whereas the right-hand panels correspond to $\sigma = 10\,000$ Pa.s m^{-2}.

the most pronounced peak of the green curve in the right-hand panel of figure 2*a* occurs) is calculated and shown in figure 2*c*. Such a quantity has been chosen because it helps in understanding how the intensity decays in space inside the material (it is zero in the air domains). The reported intensity is normalized to its value at the left-hand edge of the structure

(I_0). As additional HLs are added, the intensity decays faster, as its spatial derivative modulus is larger. This happens for both the considered study cases, although smaller values of σ (right-hand panel) appear to bring a slower decay when compared to larger values of σ (left-hand panel), a condition that implies a more efficient interaction of the acoustic wave with the structure.

Finally, figure 2*d* shows the dissipated acoustic intensity normalized to its value at the left-hand edge of the structure. Since the hierarchical design introduces additional alternating porous and air layers at different length scales, allowing the pressure field to propagate further inside the hierarchical meta-porous, the propagating wave undergoes multiple reflections while traversing the porous layers, resulting in increased dissipation. In the case of smaller value of σ, the introduction of additional HLs allows an increase in the absorption values related to the first quarter-wavelength resonance (approx. 330 Hz) and to the higher-order resonances (compare the right-hand panels of figure 2*a,d*). In contrast, when larger values of σ are considered, the field decreases more rapidly inside the structure without allowing for any noticeable geometrical resonances (left-hand panels of figure 2*a,d*).

To gain further insight on the hierarchical approach efficiency and an initial approximate estimation on the geometrical parameters for the optimization process, we can define an effective air-flow resistivity σ_{eff} as $\sigma_{eff} \sim \sigma \cdot \frac{\Sigma p_i}{p_0}$, under the hypothesis of low-frequency approximation and based on the air-flow resistivity definition. This is possible because the pressure drops are only caused by the porous media and because no bypass channels are present in the proposed designs [72,73]. In this way, we can fit the global transfer matrix method (TMM) calculations with a single layer with such an effective parameter. For instance, in the case of the third HL with HP arrangement it is possible to identify the effective sigma as $\sigma_{eff} \sim 10k \cdot p_3 \cdot 27/0.26 \sim 4.1 kNsm^{-4}$.

Figure 3 shows the comparison of the absorption coefficient for the HP configuration following: (i) the 'single layer with effective resistivity value' approach (dashed lines) and (ii) the 'TMM-based' approach (solid lines). Results are shown for the three lowest HLs (i.e. first, second and third HLs). From these comparisons, it emerges that the hierarchical approach becomes nuanced at low frequency when the material is in the homogenization regime (long wavelength), especially when low air-flow resistivity values (σ = 10 000 Pa.s m^{-2}) are considered, where the comparison is more accurate over a larger frequency range. Nevertheless, the curves of the effective single-layer approach identifies well the trend of the HP configuration (increasing absorption as additional HLs are added), indicating a good initial guess of the geometrical parameters for the optimization process.

(ii) Oblique incidence

The absorption performance depends on the angle of incidence θ of the plane wave impinging the hierarchical meta-porous under consideration, as clearly evident from equation (2.10). Figure 4*a,b* shows the absorption coefficient α at 500 Hz as a function of $\theta \in [0, 90]^\circ$ for the three HLs and the bulk block of porous material. Also in this case, two values of σ are considered (49 000 and 10 000 Pa.s m^{-2}, respectively).

The results, obtained from the transfer-matrix method (continuous coloured lines) and finite-element-based numerical simulations (circular coloured markers), clearly show that the hierarchical design is advantageous, in terms of absorption, for most of the angles of incidence, that is, $\theta \in [0^\circ, 75^\circ]$ when σ = 49 000 Pa.s m^{-2} and $\theta \in [0^\circ, 65^\circ]$ when σ = 10 000 Pa.s m^{-2}. For larger angles of incidence, the absorption curves almost merge and drop to zero when $\theta = 90^\circ$. The largest enhancement between the bulk block of porous material (0th HL) and the highest HL considered (third HL) is observed at normal incidence ($\theta = 0$), for both the values of σ, although it reaches 20% and 10% for the larger and smaller values of σ, respectively. We note that the

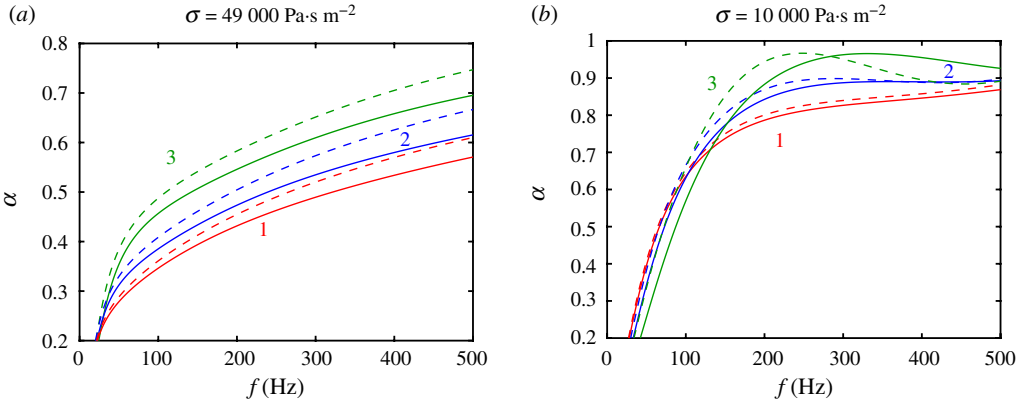

Figure 3. Effective air-flow resistivity approach (HP configuration). Comparison of the absorption coefficient for the HP configuration following: (*i*) the single layer with effective resistivity value approach (dashed lines) and (ii) the TMM-based approach (solid lines). Results are shown for the first, second and third HLs when (*a*) $\sigma = 49\,000$ Pa.s m^{-2} and (*b*) $\sigma = 49\,000$ Pa.s m^{-2} are considered, respectively.

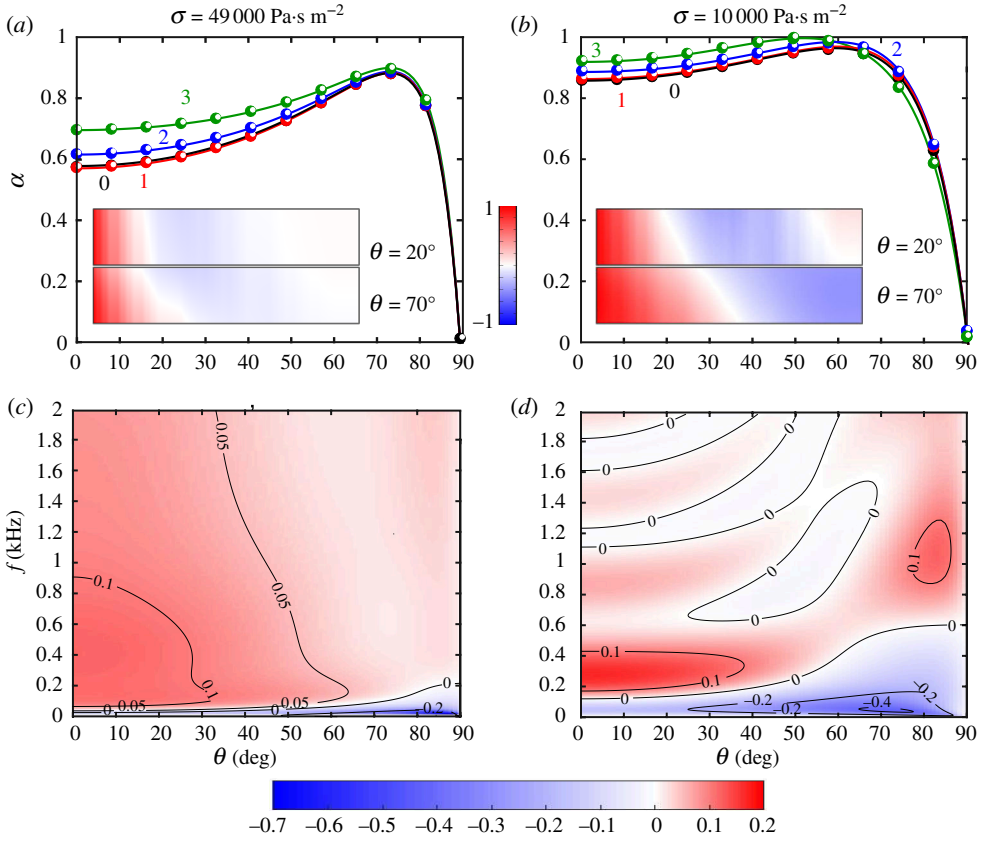

Figure 4. Influence of the angle on the absorption coefficient. (*a, b*) The absorption coefficient α at 500 Hz as a function of $\theta \in [0, 90]^\circ$ for the three HLs and the bulk block of porous material (0th HL). Different values of σ (49 000 and 10 000 Pa.s m^{-2}) are considered. The normalized total acoustic pressure fields $\frac{\Re(p)}{\max \Re(p)}$ at different angles of incidence ($\theta = 20^\circ$ and $\theta = 70^\circ$) are shown as insets. (*c, d*) The maps of the difference between the absorption coefficient α_3 of the third HL and α_0 of the 0th HL in the (f, θ) space for $\sigma = 49\,000$ and 10 000 Pa.s m^{-2}, respectively.

geometry was only optimized for normal incidence, i.e. $\theta = 0^\circ$, which, in our opinion, makes the potential of the hierarchical design remarkable since it remains advantageous also for most of the remaining angles. The normalized total acoustic pressure fields $\frac{\Re(p)}{\max \Re(p)}$ for the third HL at different angles of incidence ($\theta = 20^\circ$ and $\theta = 70^\circ$) are also shown as insets in figure 4*a*,*b*. The pressure levels reach much higher values inside the structures composed of porous media with lower values of σ, allowing for the more efficient absorption.

Extending the analysis to the other frequencies, figure 4*c*,*d* shows the maps of the difference between the absorption coefficient α_3 of the third HL and α_0 of the 0th HL in the (f, θ) space for σ = 49 000 and 10 000 Pa.s m^{-2}, respectively. The colour map has been chosen such that the regions where no enhancement of the absorption was observed (when the hierarchical design is introduced) are shown in white, whereas the regions where the hierarchy outperforms (underperforms) the bulk block porous layer are shown in dark red (blue). In this sense, larger values of σ seem to be more beneficial in the overall range of parameters, though for certain regions the smaller value of σ provides larger values of $\alpha_3 - \alpha_0$.

(iii) Influence of the static air-flow resistivity

Finally, the behaviour of $\alpha_3 - \alpha_0$ is shown in figure 5*a*,*b* as a function of the frequency f and of the static air-flow resistivity σ, when $\theta = 0^\circ$ and $\theta = 70^\circ$ (the range 10 000–50 000 Pa.s m^{-2} for σ has been considered since it corresponds to the most common values of porous media used in practical applications). The same colour map described above applies. Therefore, we can infer that, when normal incidence is considered, figure 5*a*, the enhancement of the absorption coefficient introduced by the hierarchical design (third HL compared with the bulk block of porous material) increases as the value of σ increases (except for a narrow low-frequency region). When $\theta = 70^\circ$ is considered, figure 5*b*, the frequency region within which the hierarchical design underperforms the bulk block of porous material slightly increases, especially at lower frequencies.

(b) Gradient hierarchical organization

(i) Normal incidence

Following the same approach described in §3a(iii), meta-porous media with HG organization, similar to those shown in figure 1*b*, are considered. First, the absorption coefficient α as a function of the frequency f is shown in figure 6*a*. Figure 6*b–d* shows the plots of the acoustic impedance, the spatial derivative of the acoustic intensity through the meta-porous material and the dissipated intensity maps, respectively. As in the HP case, three HLs and the bulk block of porous material are compared when σ = 49 000 Pa.s m^{-2} (left-hand panels), and when σ = 10 000 Pa.s m^{-2} (right-hand panels). The results are qualitatively and quantitatively very similar to those found for the HP organization (compare figure 2 and figure 6). Specifically, in terms of the absorption coefficient, it benefits from the introduction of hierarchy for both large and low σ study cases, though its oscillating behaviour when σ = 10 000 Pa.s m^{-2}, right-hand panel of figure 6*a*, is smoother. The impedance as a function of frequency of the HG structures exhibits a better match to the impedance of air when the smaller value of σ is considered. The intensity decays faster as the hierarchy increases for both the values of σ (figure 6*c*), leading to an increase of the absorption. Finally, the dissipated intensity normalized to the intensity at the left-hand edge of the meta-porous material at f = 600 Hz, where we observe a peak of the green curve in the right-hand panel of figure 6*a*, is shown in figure 6*d*. Also in this case, when increasing the number of HLs, the wave field propagates over a longer distance inside the material and, hence, the wave interacts with multiple porous layers getting more absorbed with

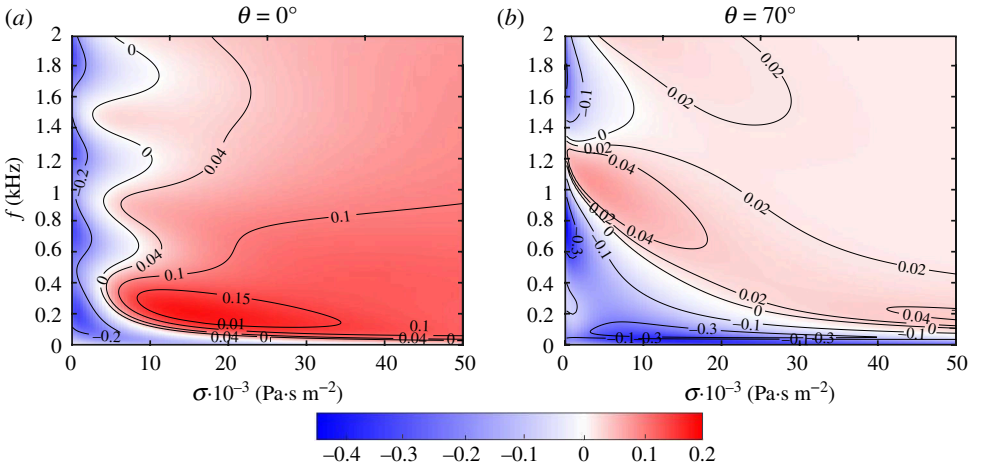

Figure 5. Influence of the static air-flow resistivity on the absorption coefficient. Difference $\alpha_3 - \alpha_0$ as a function of f and σ for (*a*) $\theta = 0°$ and (*b*) $\theta = 70°$.

respect to the non-hierarchical case. When σ = 10 000 Pa.s m^{-2}, the quarter-wavelength (approx. 200 Hz) and higher-order resonances take place. Also in this case, the hierarchy accentuates these peaks.

Note that the right-hand side excitation of the HG sample gives slightly different results with respect to the left-hand side excitation. This is due to the asymmetry of the system, as already shown in Jiménez *et al*. [34]. Nevertheless, the overall absorption efficiency is comparable. We illustrate this for the third HL (see figure 7). The difference in performance increases as the resistivity increases. Note too, that the absorption coefficient when the left-hand side excitation is considered performs better because the optimization takes into account this orientation for the incident wave. As previously done for the HP case, figure 8 reports the comparison of the absorption coefficient for the HG configuration following: (i) the 'single layer with effective resistivity value' approach (dashed lines) and (ii) the 'TMM-based' one (solid lines). Results are reported for the three lowest HLs (i.e. first, second and third HLs). Also in this case, these comparison shows that the hierarchical approach gets nuanced at low frequency when the material is in the homogenization regime (long wavelength), especially when low air flow resistivity values are considered, where the comparison is more accurate over a larger frequency range. Nevertheless, the curves of the effective single layer approach well identifies the trend of the HG configuration (increasing absorption as additional HLs are added), representing thus a good initial guess of the geometrical parameters for the optimization process.

(ii). Oblique incidence

The dependence of α on the angle of incidence is investigated and shown at f = 500 Hz in figure 9*a,b* for σ = 49 000 Pa.s m^{-2} (*a*) and σ = 10 000 Pa.s m^{-2} (*b*), respectively. Again, the introduction of hierarchy clearly shows a higher absorption coefficient in most of the angles of incidence (for both large and small values of σ), exhibiting a peak of absorption at approximately 73°. The pressure fields $\frac{\Re(p)}{\max \Re(p)}$ for $\theta = 20°$ and $\theta = 70°$ are shown in the insets of figure 9*a,b*. Their behaviour is very similar to those of the HP counterpart.

Figure 9*c,d* shows the maps of the difference between the absorption coefficient α_3 of the third HL and α_0 of the 0th HL in the (f, θ) space for σ = 49 000 and 10 000 Pa.s m^{-2}, respectively. Contrary to the HP case, when the HG organization is considered, a significant reduction of the

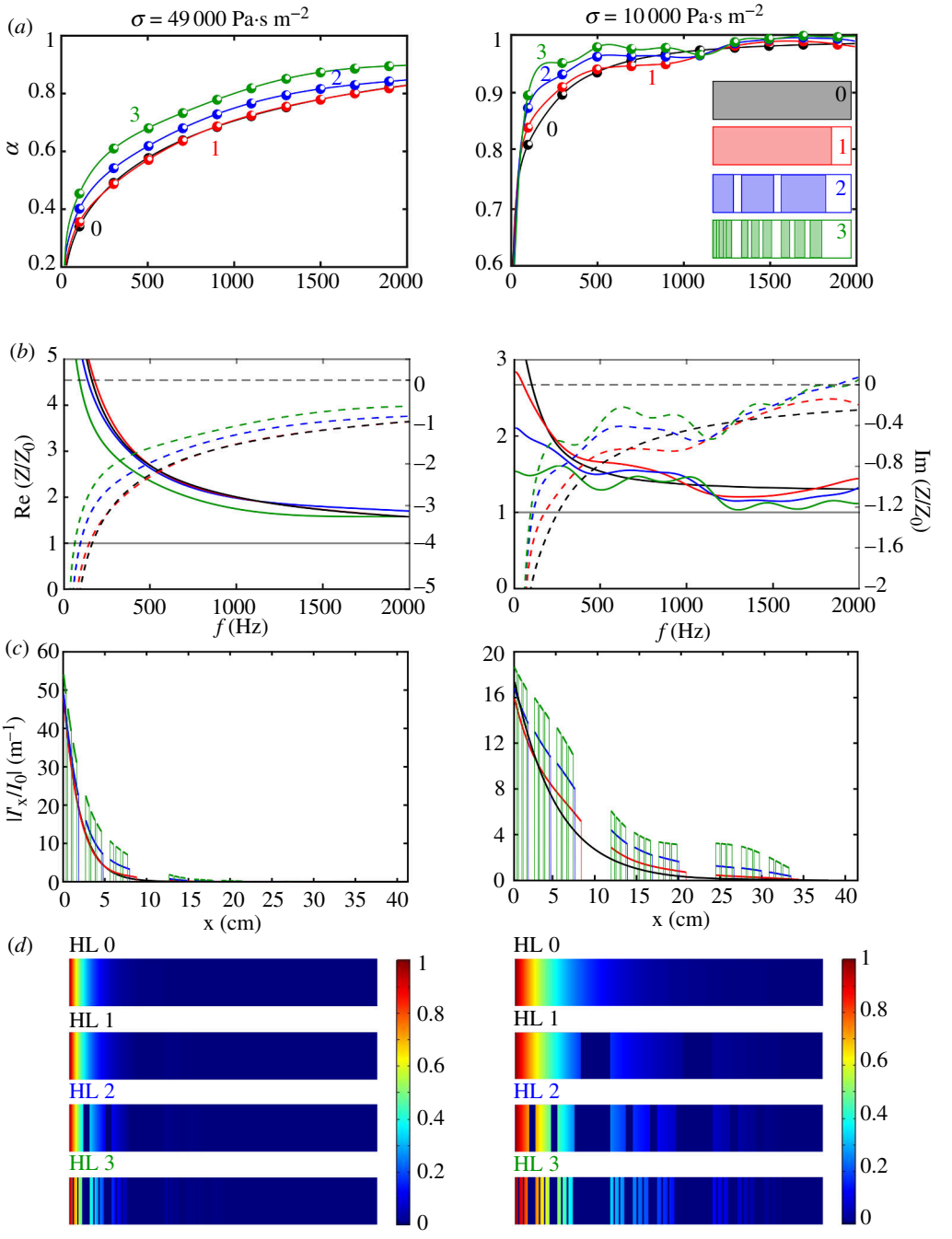

Figure 6. Absorption coefficient, impedance, spatial derivative of the acoustic intensity and the dissipated intensity. (*a*) The absorption coefficient α for different HLs, (*b*) the real (solid lines) and imaginary (dashed lines) parts of the acoustic impedance normalized to that of air, (*c*) the spatial derivative of the acoustic intensity normalized to that at the left-hand end of the structure at $f = 600$ Hz, and (*d*) the dissipated intensity at $f = 600$ Hz. The left-hand panels correspond to $\sigma = 49\,000$ Pa.s m^{-2}, while the right-hand ones correspond to $\sigma = 10\,000$ Pa.s m^{-2}.

low-frequency region where the hierarchical design was underperforming with respect to the bulk block is observed.

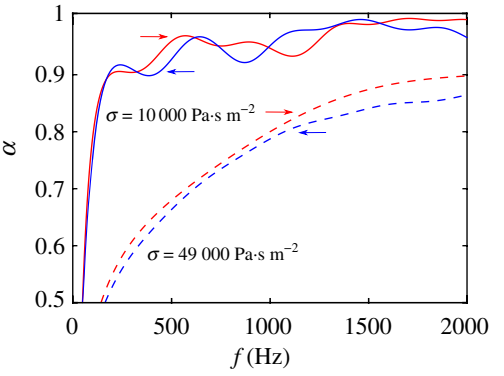

Figure 7. Comparison of the right- and left-hand side incidence. Third HL performance of the HG sample under the left- and right-hand side normal incidence.

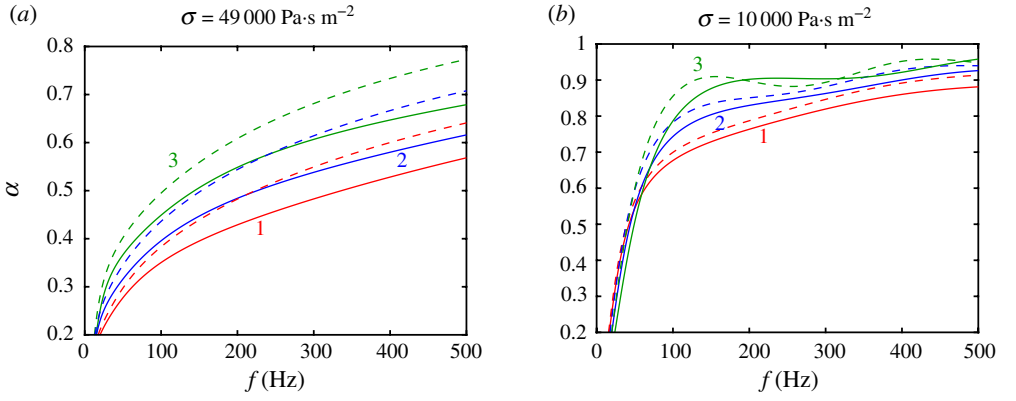

Figure 8. Effective air-flow resistivity approach (HG configuration). Comparison of the absorption coefficient for the HG configuration following: (i) the single layer with effective resistivity value approach (dashed lines) and (ii) the TMM-based one (solid lines). Results are shown for the first, second and third HLs when (*a*) $\sigma = 49\,000$ Pa.s m^{-2} and (*b*) $\sigma = 10\,000$ Pa.s m^{-2} is considered, respectively.

(iii). Influence of the static air-flow resistivity

Finally, the behaviour of $\alpha_3 - \alpha_0$ as a function of the frequency f and of the static air-flow resistivity σ for $\theta = 0^\circ$ and $\theta = 70^\circ$ is shown in figure 10*a*,*b*, respectively. Most of the (σ, f) combinations show that the introduction of the hierarchy is beneficial in terms of absorption. The overall increase of α is more consequent in the case of normal incidence (α being twice as large than for $\theta = 70^\circ$ at the peak values).

Figure 11 shows the comparison of the absorption coefficient of the HP and HG samples for (*a*) normal and (*b*) oblique incidence. When large values of σ are considered the performance is almost the same for both samples and the curves of the absorption coefficients barely differs. When small values of σ are considered, the oscillating behaviour of the curves allows to identify some frequency ranges where one type of hierarchy is performing better than the other. Nevertheless, we can say that the overall performances of the HP and HG organizations are comparable.

4. Experimental results

To experimentally validate our approach, HP and HG specimens were manufactured by assembling water-jet cut cylinders of Agglo 80 made of polyurethane foam as shown in the

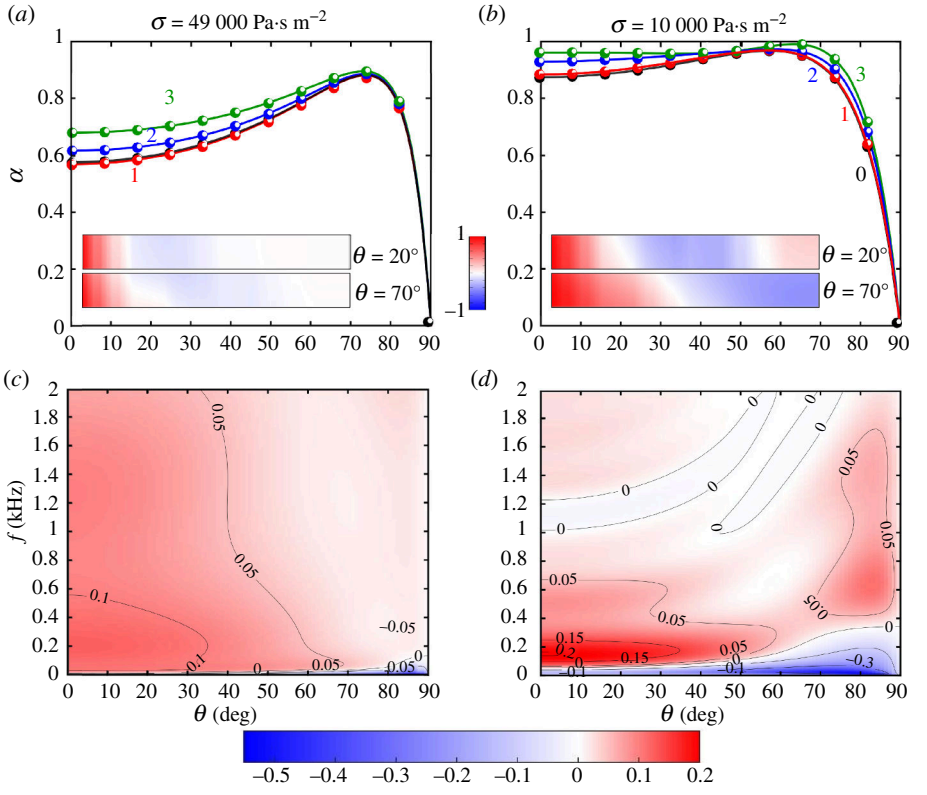

Figure 9. Influence of the angle on the absorption coefficient. (*a, b*) The absorption coefficient α at 500 Hz as a function of $\theta \in [0, 90]^\circ$ for the three HLs and the bulk block of porous material (0th HL). Different values of σ (49 000 and 10 000 Pa.s m^{-2}) are considered. The normalized total acoustic pressure fields $\frac{\Re(p)}{\max \Re(p)}$ at different angles of incidence ($\theta = 20^\circ$ and $\theta = 70^\circ$) are shown as insets. (*c, d*) The maps of the difference between the absorption coefficient α_3 of the third HL and α_0 of the 0th HL in the (f, θ) space for $\sigma = 49\,000$ and 10 000 Pa.s m^{-2}, respectively.

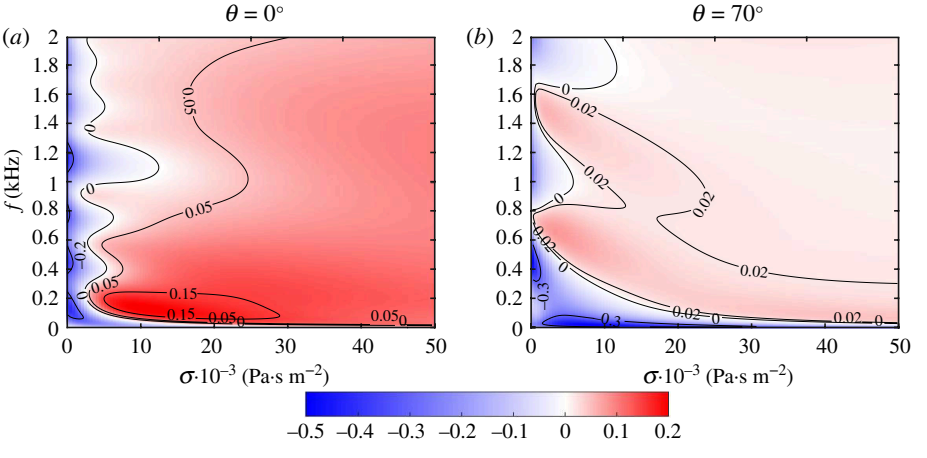

Figure 10. Influence of the static air-flow resistivity on the absorption coefficient. Difference $\alpha_3 - \alpha_0$ as a function of f and σ for (*a*) $\theta = 0^\circ$ and (*b*) $\theta = 70^\circ$.

schematics in figure 1. Their absorption coefficient was measured via a reflection experiment into an impedance tube using the 'two microphone technique' (standard ISO 10534–2). The

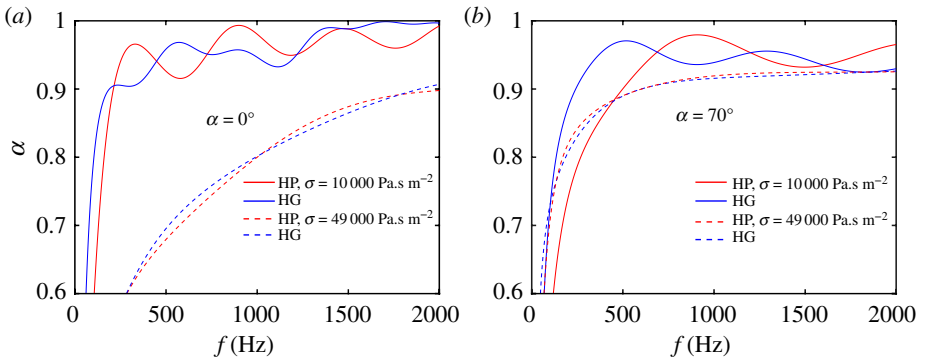

Figure 11. Comparison of HP and HG performances. Absorption of the third level of HP and GP at (*a*) normal and (*b*) oblique incidence.

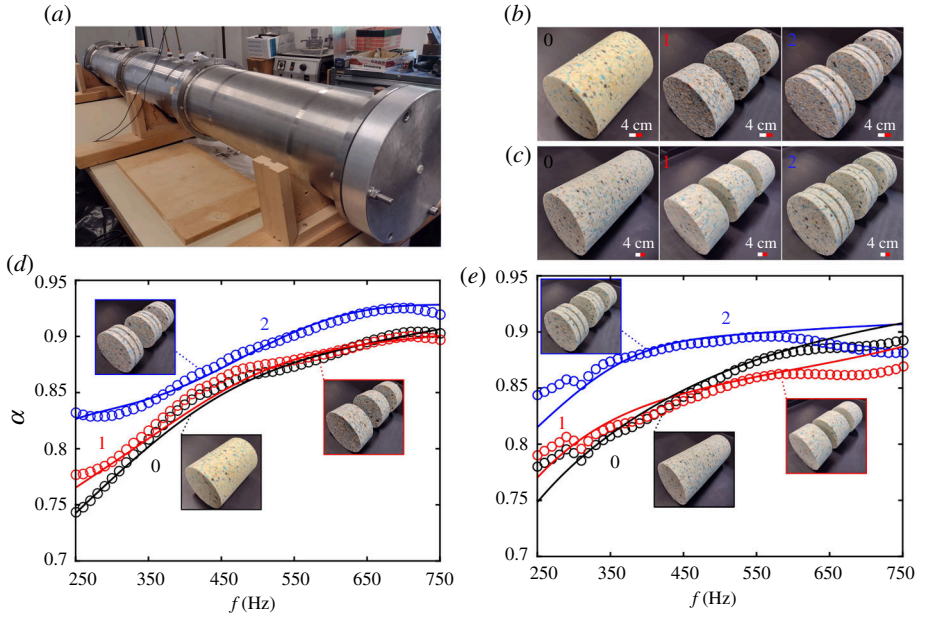

Figure 12. Experimental results. (*a*) Photograph of the experimental set-up. (*b, c*) Photographs of the examined samples, i.e. the 0th, first and second HLs for the HP and HG organization, respectively. (*d*) Calculated (solid lines) and measured (circles) absorption coefficients for the HP samples. (*e*) Calculated (solid lines) and measured (circles) absorption coefficients for the HG samples.

following nominal properties for Agglo 80 have been adopted: $\sigma = 12\ 550$ Pa.s m^{-2}, $\phi = 0.93$, $\Lambda = 57\ \mu m$, $\Lambda' = 125\ \mu m$, $\alpha_\infty = 1.08$.

A photograph of the experimental set-up, reliably operating in the 250–750 Hz range, is shown in figure 12*a*. It consists of: (i) a laboratory-made impedance tube of length 190 cm and diameter 19.2 cm, (ii) four loudspeakers Visaton FRS of diameter of 50 mm linked to (iii) an amplifier Bruel et Kjaer of type 2706 and (iv) two Sennheiser MKE 2P microphones.

Figure 12*b,c* shows the photographs of the examined samples, i.e. the 0th, first and second HLs for the HP and HG organization, respectively, while results are presented in figure 12*d*. Measurements, reported as the coloured circular markers, are superimposed on the analytical prediction (solid coloured lines). Excellent agreement is found, confirming the trend of enhanced absorption properties with the increase of the HL. Note, that we decided not to measure the third HL owing to the unfavourable ratio of the thickness of the porous layers required (4 mm) and the diameter of the tube (192 mm), which presented additional

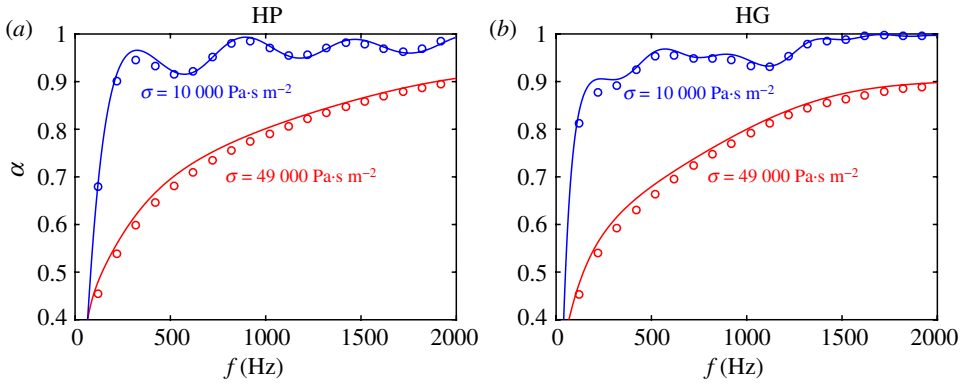

Figure 13. Influence of the disorder. Absorption coefficient of the third HL for the (*a*) HP and (*b*) HG configurations when no disorder is considered in the arrangement of the porous layers (continuous lines). Circular markers indicate, instead, the absorption coefficient when random variation of the widths of the layers (up to 30%) is considered. Blue and red colours indicate the results for low and high values of σ, respectively.

difficulties to properly hold the samples in the tube. Nevertheless, as discussed in the following, the measurements for the 0th, first and second HLs show a very good agreement with the calculations, confirming the anticipated trend. We leave the problem of how to properly assemble the third HL for our future research.

For the sake of completeness, the robustness of the improvement owing to the hierarchical design when introducing thickness errors in the individual slabs of the porous layers is also examined. Specifically, the absorption coefficient of the HP and HG periodic patterns is calculated when a random error (up to 30%) at the level of the thicknesses of the layers keeping their position (middle cross-section) unaltered and avoiding material overlapping (figure 13). We can clearly see that the improvements owing to hierarchy are rather robust with respect to the random relative deviation from the initial thicknesses of the layers.

5. Conclusions

We have investigated numerically and experimentally the absorption coefficient of a hierarchical meta-porous media made of alternating porous and air layers. The numerical studies were based both on the analytical formalism and on the finite-element method. The measurements were performed at normal incidence in an impedance tube.

Two designs have been proposed: the HP and HG. Both structures have been shown to exhibit advantageous absorbing properties in some frequencies within the 20–2000 Hz range compared to a block of porous material of the same length. A maximum enhancement of 39% was observed in the hierarchical periodic organization. The proposed designs also introduced porous volume reductions (with respect to the 100% porous material of the 0th HL as follows: 17% for the first HL, 37.7% for the second HL, 58.5% for the third HL in the HP organization and 28.6% for the first HL, 47% for the second HL, 58.7% for the third HL in the HG study case.

The chosen geometrical parameters found from the optimization were revealed to be distributed smoothly with respect to the variation of the porous and air lengths. This confirms the robustness of the hierarchical design with respect to potential geometrical imperfections resulting from the manufacturing process.

In addition, the hierarchical geometries, optimized for a single value of static air-flow resistivity (σ) and for normal wave incidence ($\theta = 0$) only, remained remarkably advantageous (exhibiting higher absorption) for a wide range of angles of incidence and static air-flow resistivity. Specifically, when large values of σ are considered, a gradual increase of the absorption coefficient as additional HLs are added was observed for both the periodic and

gradient designs. The largest enhancement of the absorption coefficient is, however, observed at normal incidence.

The proposed hierarchical meta-porous material was shown to be a promising design for increasing the low-frequency sound absorption of porous media, exploitable in most of the noise shielding applications related to human activities, such as room acoustics, engine noise control and, in general, where the space to host the absorber is limited. Another advantage of using this approach is on the fabrication, since only one porous material is required.

The experiments provided can be considered as a proof of concept for the normal incidence case.

Data accessibility. The codes and data are available online as supplementary material [74].

Declaration of AI use. We have not used AI-assisted technologies in creating this article.

Authors' contributions. S.K.: conceptualization, formal analysis, investigation, methodology, writing—original draft, writing—review and editing; S.D.: formal analysis, investigation, methodology, writing—review and editing; F.A.: data curation, investigation; B.D.: conceptualization, methodology, supervision, writing—review and editing; M.M.: conceptualization, formal analysis, funding acquisition, investigation, methodology, project administration, resources, supervision, writing—original draft, writing—review and editing.

All authors gave final approval for publication and agreed to be held accountable for the work performed therein.

Conflict of interest declaration. We declare we have no competing interests.

Funding. S.K. and M.M. are supported by the European Union's Horizon 2020 programme in the framework of the FET Open « BOHEME: Bio-Inspired Hierarchical Metamaterials » (Grant Agreement no. 863179).

References

1. Bies DA, Hansen CH. *Engineering noise control*. CRC press. (doi:10.1201/9781315273464)
2. Paris E. 1927 On the reflexion of sound from a porous surface. *Proc. R. Soc. Lond. A* **115**, 407–419. (doi:10.1098/rspa.1927.0100)
3. Göransson P. 2006 Acoustic and vibrational damping in porous solids. *Phil. Trans. R. Soc. A.* **364**, 89–108. (doi:10.1098/rsta.2005.1688)
4. Wang Y, Wang Y, Xu J, Yu H, Zhang C, Ren L. 2021 Broadband low-frequency sound absorption by coiled-up space embedded in a porous layer. *Appl. Acoust.* **182**, 108226. (doi:10.1016/j.apacoust.2021.108226)
5. Biot MA. 1956 Theory of propagation of elastic waves in a fluid-saturated porous solid. I. low-frequency range. *J. Acoust. Soc. Am.* **28**, 168–178. (doi:10.1121/1.1908239)
6. Biot MA. 1956 Theory of propagation of elastic waves in a fluid-saturated porous solid. II. higher frequency range. *J. Acoust. Soc. Am.* **28**, 179–191. (doi:10.1121/1.1908241)
7. Allard JF, Aknine A, Depollier C. 1986 Acoustical properties of partially reticulated foams with high and medium flow resistance. *J. Acoust. Soc. Am.* **79**, 1734–1740. (doi:10.1121/1.393234)
8. Johnson DL, Koplik J, Dashen R. 1987 Theory of dynamic permeability and tortuosity in fluid-saturated porous media. *J. Fluid Mech.* **176**, 379. (doi:10.1017/S0022112087000727)
9. Jiménez N, Umnova O, Groby JP. 2021 Acoustic waves in periodic structures, metamaterials, and porous media. In *Ch. the transfer matrix method in acoustics*, pp. 103–164. Cham: Springer International Publishing. (doi:10.1007/978-3-030-84300-7_4)
10. Cox T, d'Antonio P. 2016 *Acoustic absorbers and diffusers: theory, design and application*. Boca Raton, FL: CRC press.
11. Allard J, Atalla N. 2009 *Propagation of sound in porous media: modelling sound absorbing materials*. Chichester, UK: John Wiley & Sons.
12. Cao L, Fu Q, Si Y, Ding B, Yu J. 2018 Porous materials for sound absorption. *Comp. Commun.* **10**, 25–35. (doi:10.1016/j.coco.2018.05.001)
13. Gao N, Zhang Z, Deng J, Guo X, Cheng B, Hou H. 2022 Acoustic metamaterials for noise reduction: a review. *Adv. Mater. Technol.* **7**, 2100698. (doi:10.1002/admt.202100698)

14. Groby JP, Lagarrigue C, Brouard B, Dazel O, Tournat V, Nennig B. 2015 Enhancing the absorption properties of acoustic porous plates by periodically embedding helmholtz resonators. *J. Acoust. Soc. Am.* **137**, 273–280. (doi:10.1121/1.4904534)
15. Lagarrigue C, Groby JP, Tournat V, Dazel O, Umnova O. 2013 Absorption of sound by porous layers with embedded periodic arrays of resonant inclusions. *J. Acoust. Soc. Am.* **134**, 4670–4680. (doi:10.1121/1.4824843)
16. Zhu XF, Lau SK, Lu Z, Jeon W. 2019 Broadband low-frequency sound absorption by periodic metamaterial resonators embedded in a porous layer. *J. Sound Vib.* **461**, 114922. (doi:10.1016/j.jsv.2019.114922)
17. Yang J, Lee JS, Kim YY. 2015 Metaporous layer to overcome the thickness constraint for broadband sound absorption. *J. Appl. Phys.* **117**, 17. (doi:10.1063/1.4919844)
18. Yang J, Lee JS, Kim YY. 2017 Multiple slow waves in metaporous layers for broadband sound absorption. *J. Phys. D. Appl. Phys.* **50**, 015301. (doi:10.1088/1361-6463/50/1/015301)
19. Li D, Chang D, Liu B. 2017 Enhanced low- to mid-frequency sound absorption using parallel-arranged perforated plates with extended tubes and porous material. *Appl. Acoust.* **127**, 316–323. (doi:10.1016/j.apacoust.2017.06.019)
20. Liu X, Yu C, Xin F. 2021 Gradually perforated porous materials backed with helmholtz resonant cavity for broadband low-frequency sound absorption. *Compos. Struct.* **263**, 113647. (doi:10.1016/j.compstruct.2021.113647)
21. Toyoda M, Sakagami K, Okano M, Okuzono T, Toyoda E. 2017 Improved sound absorption performance of three-dimensional MPP space sound absorbers by filling with porous materials. *Appl. Acoust.* **116**, 311–316. (doi:10.1016/j.apacoust.2016.10.006)
22. Liu Z, Zhan J, Fard M, Davy JL. 2017 Acoustic measurement of a 3D printed micro-perforated panel combined with a porous material. *Meas. Lond.* **104**, 233–236. (doi:10.1016/j.measurement.2017.03.032)
23. Xin F, Ma X, Liu X, Zhang C. 2019 A multiscale theoretical approach for the sound absorption of slit-perforated double porosity materials. *Compos. Struct.* **223**, 110919. (doi:10.1016/j.compstruct.2019.110919)
24. Attenborough K. 2021 Analytical approximations for sub wavelength sound absorption by porous layers with labyrinthine slit perforations. *Appl. Sci.* **11**, 3299. (doi:10.3390/app11083299)
25. Atalla N, Panneton R, Sgard FC, Olny X. 2001 Acoustic absorption of macro-perforated porous materials. *J. Sound Vib.* **243**, 659–678. (doi:10.1006/jsvi.2000.3435)
26. Dunn IP, Davern WA. 1986 Calculation of acoustic impedance of multi-layer absorbers. *Appl. Acoust.* **19**, 321–334. (doi:10.1016/0003-682X(86)90044-7)
27. Lauriks W, Mees P, Allard JF. 1992 The acoustic transmission through layered systems. *J. Sound Vib.* **155**, 125–132. (doi:10.1016/0022-460X(92)90650-M)
28. Brouard B, Lafarge D, Allard JF. 1995 A general method of modelling sound propagation in layered media. *J. Sound Vib.* **183**, 129–142. (doi:10.1006/jsvi.1995.0243)
29. Craster RV, Guenneau S. 2012 *Acoustic metamaterials: negative refraction, imaging, lensing and cloaking*. Dordrecht, Heidelberg, New York, London: Springer Science & Business Media. (doi:10.1007/978-94-007-4813-2)
30. Romero-Garcia V, Hladky-Hennion AC. 2019 *Fundamentals and applications of acoustic metamaterials: from seismic to radio frequency*. London, UK: John Wiley & Sons.
31. Ghaffari Mosanenzadeh S, Naguib HE, Park CB, Atalla N. 2015 Design and development of novel bio-based functionally graded foams for enhanced acoustic capabilities. *J. Mater. Sci.* **50**, 1248–1256. (doi:10.1007/s10853-014-8681-6)
32. Zhang X, Qu Z, Wang H. 2020 Engineering acoustic metamaterials for sound absorption: from uniform to gradient structures. *iScience* **23**, 101110. (doi:10.1016/j.isci.2020.101110)
33. Roca D, Cante J, Lloberas-Valls O, Pàmies T, Oliver J. 2021 Multiresonant layered acoustic metamaterial (MLAM) solution for broadband low-frequency noise attenuation through double-peak sound transmission loss response. *Extreme Mech. Lett.* **47**, 101368. (doi:10.1016/j.eml.2021.101368)
34. Jiménez N, Romero-García V, Cebrecos A, Picó R, Sánchez-Morcillo VJ, Garcia-Raffi LM. 2016 Broadband quasi perfect absorption using chirped multi-layer porous materials. *AIP Adv.* **6**. (doi:10.1063/1.4971274)

35. Jiménez N, Romero-García V, Groby JP. 2018 Perfect absorption of sound by rigidly-backed high-porous materials. *Acta Acust. United Acust.* **104**, 396–409. (doi:10.3813/AAA.919183)
36. Bécot FX, Jaouen L, Gourdon E. 2008 Applications of the dual porosity theory to irregularly shaped porous materials. *Acta Acust. United Acust.* **94**, 715–724. (doi:10.3813/AAA.918088)
37. Sgard FC, Olny X, Atalla N, Castel F. 2005 On the use of perforations to improve the sound absorption of porous materials. *Appl. Acoust.* **66**, 625–651. (doi:10.1016/j.apacoust.2004.09.008)
38. Almeida G do N, Vergara EF, Lenzi A, Alves ÁS, de Jesus JCO. 2023 Low-frequency broadband sound absorption based on Cantor fractal porosity. *J. Appl. Phys.* **133**, 23. (doi:10.1063/5.0150998)
39. Song GY, Cheng Q, Huang B, Dong HY, Cui TJ. 2016 Broadband fractal acoustic metamaterials for low-frequency sound attenuation. *Appl. Phys. Lett.* **109**, 131901. (doi:10.1063/1.4963347)
40. Mousanezhad D, Babaee S, Ebrahimi H, Ghosh R, Hamouda AS, Bertoldi K, Vaziri A. 2015 Hierarchical honeycomb auxetic metamaterials. *Sci. Rep.* **5**, 18306. (doi:10.1038/srep18306)
41. Miniaci M, Krushynska A, Gliozzi AS, Kherraz N, Bosia F, Pugno NM. 2018 Design and fabrication of bioinspired hierarchical dissipative elastic metamaterials. *Phys. Rev. Appl.* **10**, 024012. (doi:10.1103/PhysRevApplied.10.024012)
42. Dal Poggetto VF. 2023 Bioinspired acoustic metamaterials: from natural designs to optimized structures. *Front. Mater.* **10**, 1176457. (doi:10.3389/fmats.2023.1176457)
43. Neil TR, Shen Z, Robert D, Drinkwater BW, Holderied MW. 2022 Moth wings as sound absorber metasurface. *Proc. Math. Phys. Eng. Sci.* **478**, 20220046. (doi:10.1098/rspa.2022.0046)
44. Wang YT, Shen Z, Neil TR, Holderied MW, Skelton EA, Craster RV. 2022 Models for resonant acoustic metasurfaces with application to moth wing ultrasound absorption. *Philos. Trans. A. Math. Phys. Eng. Sci.* **380**, 20220005. (doi:10.1098/rsta.2022.0005)
45. Davies B, Herren L. 2022 Robustness of subwavelength devices: a case study of cochlea-inspired rainbow sensors. *Proc. Math. Phys. Eng. Sci.* **478**, 20210765. (doi:10.1098/rspa.2021.0765)
46. Lakes R. 1993 Materials with structural hierarchy. *Nature* **361**, 511–515. (doi:10.1038/361511a0)
47. Li X, Yu X, Zhao M, Li Z, Wang Z, Zhai W. 2023 Multi-level bioinspired microlattice with broadband sound-absorption capabilities and deformation-tolerant compressive response. *Adv. Funct. Mater.* **33**, 2210160. (doi:10.1002/adfm.202210160)
48. Ruan H, Li D. 2022 Wave propagation properties of a spider-web-like hierarchical acoustic metamaterial. *Phys. Status Solidi* **259**, 2200341. (doi:10.1002/pssb.202200341)
49. Sun P, Zhang Z, Guo H, Liu N, Jin W, Yuan T, Wang Y. 2022 Topological optimization of hierarchical honeycomb acoustic metamaterials for low-frequency extreme broad band gaps. *Appl. Acoust.* **188**, 108579. (doi:10.1016/j.apacoust.2021.108579)
50. Ma N, Han Q, Han S, Li C. 2023 Hierarchical re-entrant honeycomb metamaterial for energy absorption and vibration insulation. *Int. J. Mech. Sci.* **250**, 108307. (doi:10.1016/j.ijmecsci.2023.108307)
51. Edwards WT, Chang CM, McKnight G, Sorensen A, Nutt SR. 2020 Transmission loss and dynamic response of hierarchical membrane-type acoustic metamaterials. *J. Vib. Acoust.* **142**, 021007. (doi:10.1115/1.4045789)
52. He W, Peng X, Xin F, Lu TJ. 2022 Ultralight micro-perforated sandwich panel with hierarchical honeycomb core for sound absorption. *J. Sandwich Struct. Mater.* **24**, 201–217. (doi:10.1177/1099636221993880)
53. Man X, Xia B, Luo Z, Liu J, Li K, Nie Y. 2021 Engineering three-dimensional labyrinthine fractal acoustic metamaterials with low-frequency multi-band sound suppression. *J. Acoust. Soc. Am.* **149**, 308–319. (doi:10.1121/10.0003059)
54. Krushynska AO, Bosia F, Miniaci M, Pugno NM. Spider web-structured labyrinthine acoustic metamaterials for low-frequency sound control. *New J. Phys.* **19**, 105001. (doi:10.1088/1367-2630/aa83f3)
55. Dunckley L, Davies B. 2024 Hierarchical band gaps in complex periodic systems. *C. R. Mécanique.* **352**, 143–157. (doi:10.5802/crmeca.249)

56. Mazzotti M, Foehr A, Bilal OR, Bergamini A, Bosia F, Daraio C, Pugno NM, Miniaci M. 2023 Bio-inspired non self-similar hierarchical elastic metamaterials. *Int. J. Mech. Sci.* **241**, 107915. (doi:10.1016/j.ijmecsci.2022.107915)
57. Zhang P, To AC. 2013 Broadband wave filtering of bioinspired hierarchical phononic crystal. *Appl. Phys. Lett.* **102**, 12. (doi:10.1063/1.4799171)
58. Fratzl P, Weinkamer R. 2007 Nature's hierarchical materials. *Prog. Mater. Sci.* **52**, 1263–1334. (doi:10.1016/j.pmatsci.2007.06.001)
59. Meza LR, Zelhofer AJ, Clarke N, Mateos AJ, Kochmann DM, Greer JR. 2015 Resilient 3D hierarchical architected metamaterials. *Proc. Natl Acad. Sci. USA* **112**, 11502–11507. (doi:10.1073/pnas.1509120112)
60. Calvert P, Cesarano J, Chandra H, Denham H, Kasichainula S, Vaidyanathan R. 2002 Toughness in synthetic and biological multilayered systems. *Philos. Trans. R. Soc. Lond. Ser. A. Math. Phys. Eng. Sci.* **360**, 199–209. (doi:10.1098/rsta.2001.0925)
61. Petkovich N, Stein A, Su B, Sanchez C, Yang X. Hierarchically structured porous materials: from nanoscience to catalysis, separation, optics, energy and life science (doi:10.1002/9783527639588)
62. Askarinejad S, Rahbar N. 2015 Toughening mechanisms in bioinspired multilayered materials. *J. R. Soc. Interface* **12**, 20140855. (doi:10.1098/rsif.2014.0855)
63. Weaver JC *et al.* 2012 The stomatopod dactyl club: a formidable damage-tolerant biological hammer. *Science* **336**, 1275–1280. (doi:10.1126/science.1218764)
64. De Ryck L, Groby JP, Leclaire P, Lauriks W, Wirgin A, Fellah ZEA, Depollier C. 2007 Acoustic wave propagation in a macroscopically inhomogeneous porous medium saturated by a fluid. *Appl. Phys. Lett.* **90**. (doi:10.1063/1.2431570)
65. Champoux Y, Allard JF. 1991 Dynamic tortuosity and bulk modulus in air-saturated porous media. *J. Appl. Phys.* **70**, 1975–1979. (doi:10.1063/1.349482)
66. Groby JP, Dazel O, Duclos A, Boeckx L, Kelders L. 2011 Enhancing the absorption coefficient of a backed rigid frame porous layer by embedding circular periodic inclusions. *J. Acoust. Soc. Am.* **130**, 3771–3780. (doi:10.1121/1.3652865)
67. Allard JF, Champoux Y. 1992 New empirical equations for sound propagation in rigid frame fibrous materials. *J. Acoust. Soc. Am.* **91**, 3346–3353. (doi:10.1121/1.402824)
68. Pride SR, Morgan FD, Gangi AF. 1993 Drag forces of porous-medium acoustics. *Phys. Rev. B* **47**, 4964–4978. (doi:10.1103/PhysRevB.47.4964)
69. Feo TA, Resende MGC. 1995 Greedy randomized adaptive search procedures. *J. Glob. Optim.* **6**, 109–133. (doi:10.1007/BF01096763)
70. Holland JH. 1992 *Adaptation in natural and artificial systems: an introductory analysis with applications to biology, control, and artificial intelligence*. Cambridge, MA: MIT press.
71. Kennedy J, Eberhart R. 1995 Particle swarm optimization. In *ICNN'95 - International Conference on Neural Networks*, Perth, WA, Australia, vol. **4**, pp. 1942–1948, (doi:10.1109/ICNN.1995.488968)
72. Olny X, Boutin C. 2003 Acoustic wave propagation in double porosity media. *J. Acoust. Soc. Am.* **114**, 73–89. (doi:10.1121/1.1534607)
73. Venegas R, Boutin C, Umnova O. 2017 Acoustics of multiscale sorptive porous materials. *Phys. Fluids* **29**, 8. (doi:10.1063/1.4999053)
74. Kuznetsova S, Deleplanque S, Allein F, Dubus B, Miniaci M. 2024 Data from: Hierarchical meta-porous materials as sound absorbers. Figshare. (doi:10.6084/m9.figshare.c.7477906)